Article

Multi-Channel Exploration of O Adatom on TiO$_2$(110) Surface by Scanning Probe Microscopy

Huan Fei Wen [1,2] , Yasuhiro Sugawara [1,2] and Yan Jun Li [2,*]

[1]   Key Laboratory of Instrumentation Science and Dynamic Measurement, School of Instrument and
    Electronics, North University of China, Taiyuan 030051, China; wenhuanfei@nuc.edu.cn (H.F.W.);
    sugawara@ap.eng.osaka-u.ac.jp (Y.S.)
[2]   Department of Applied Physics, Graduate School of Engineering, Osaka University, 2-1 Yamadaoka, Suita,
    Osaka 565-0871, Japan
[*]   Correspondence: liyanjun@ap.eng.osaka-u.ac.jp

check for
updates

Abstract: We studied the O$_2$ dissociated state under the different O$_2$ exposed temperatures with
atomic resolution by scanning probe microscopy (SPM) and imaged the O adatom by simultaneous
atomic force microscopy (AFM)/scanning tunneling microscopy (STM). The effect of AFM operation
mode on O adatom contrast was investigated, and the interaction of O adatom and the subsurface
defect was observed by AFM/STM. Multi-channel exploration was performed to investigate the
charge transfer between the adsorbed O and the TiO$_2$(110) by obtaining the frequency shift, tunneling
current and local contact potential difference at an atomic scale. The tunneling current image showed
the difference of the tunneling possibility on the single O adatom and paired O adatoms, and the local
contact potential difference distribution of the O-TiO$_2$(110) surface institutively revealed the charge
transfer from TiO$_2$(110) surface to O adatom. The experimental results are expected to be helpful in
investigating surface/interface properties by SPM.

Keywords: multi-channel; surface property; scanning probe microscopy

1. Introduction

Scanning probe microscopy (SPM) has developed as a powerful tool for exploring the surface
properties and surface dynamic process at an atomic scale on a semiconductor or insulator [1–10].
For example, atomic manipulation has been realized, and surface chemical reactions have been
observed with atomic resolution by atomic force microscopy (AFM). Based on AFM, Kelvin probe force
microscopy (KPFM) was developed to characterize the contact potential difference (CPD) between
the substrate and cantilever tip. CPD originates from the difference of the work functions and is
specifically referred to as the local CPD (LCPD) in atomic-resolution KPFM [11,12]. To date, different
modes of KPFM have been successfully used to simultaneously measure surface structures and LCPD,
and the surface potential of TiO$_2$(110) was measured [13–19]. Local density of states (LDOS) gives
significant information of the electronic structure of the surface, which is measured by scanning
tunneling microscopy (STM). Combining AFM/STM techniques has been developed to investigate
the surface structure and LDOS [20–22]. Simultaneous measurement of tunneling current and LCPD
is useful to explore the surface properties and surface reaction process, but it cannot be achieved by
the conventional KPFM due to the regulation of DC bias voltage. To simultaneously characterize
the electronic structure and LCPD, we previously proposed a method to achieve the frequency shift
(Δf), average tunneling current ($<I_t>$) and LCPD by the KPFM without DC bias voltage feedback,
and this method was successfully performed on the rutile TiO$_2$(110) surface [19]. Hence, based on

AFM, multi-channel exploration has the potential to explore the charge transfer of the interface and to unravel physical features for understanding the surface catalytic process.

Oxygen molecular interaction with TiO_2 has attracted much attention and has become a prototypical model due to its importance in many surface reactions. Molecular oxygen acts as the main oxidizing reagent in many catalytic reactions and is used as an electron scavenger, which is believed to facilitate surface reactions. The adsorption and dissociation of O_2 on the rutile $TiO_2(110)$ surface at low and room temperatures have been well characterized by STM experimental and theoretical study, where the oxygen molecular adsorbed on the Ti_{5c} site or the surface bridging oxygen vacancies (O_v) and the oxygen adatom (O_{ad}) along the fivefold-coordinated Ti_{5c} site is formed [23,24]. Importantly, it is believed that chemical adsorption and dissociation of O_2 on the TiO_2 surface accompanied by the charge transfer and the activation of O_2 dissociation are key factors in the reaction process, which is importantly related to their charge state. Therefore, multi-channel exploring of the state of O_{ad} on $TiO_2(110)$ surface is useful in understanding its fundamental mechanism.

In this study, we first showed the dissociation state of O_{ad} on the $TiO_2(110)$ surface under the different O_2-exposed temperatures by AFM, and then we characterized the O_{ad} by simultaneous AFM/STM, which would provide complementary information in recording the topographic and tunneling current signals. Finally, simultaneous measurements of frequency shift, tunneling current and LCPD images on the O-$TiO_2(110)$ surface are taken by SPM. The tunneling current contrast and surface potential difference were analyzed to explore the charge transfer between the O_{ad} and TiO_2 surface. The experimental results and methods are useful in characterizing the other nanomaterials.

2. Experimental Details

Experiments were performed with a home-built no contact (NC)-AFM system under ultrahigh vacuum conditions (3×10^{-11} Torr) at 78 K, which was operated in frequency modulation (FM). An AFM cantilever was oscillated at a constant amplitude and at its resonant frequency by automatic gain control (AGC). AFM/STM simultaneous measurements can be carried out in two ways, and force signal and tunneling current are recorded in the separated channel. When the frequency shift was operated as the feedback signal, topographic and $<I_t>$ images were simultaneously recorded and $<I_t>$ contained crosstalk of tip motion. When measurements were taken in the constant height mode, frequency shift and $<I_t>$ could be simultaneously obtained. In this mode, two signals were independently measured, so they did not contain the artificial signal. The comparison of two operation modes will be shown in the results section. Figure 1 shows the experimental setup for simultaneous measurements of topography, $<I_t>$ and LCPD. Topography and $<I_t>$ images were obtained by AFM, and LCPD images were recorded by FM-KPFM in the constant height mode. The equation for V_{LCPD} was derived as follows; details can be found in Ref. [18,19]:

$$V_{LCPD} = V_{DC} - \text{sgn}(\alpha_m) \frac{V_{ac}}{4} \frac{|\Delta f_m|}{|\Delta f_{2m}|} \frac{T(f_{2m})}{T(f_m)} \tag{1}$$

Here, V_{DC} is the dc voltage. The parameter $\text{sgn}(\alpha_m)$ is known by the phase difference between V_{ac} and $|\Delta f_m|$. $|\Delta f_m|$ and $|\Delta f_{2m}|$ are the f_m and f_{2m} components of Δf, respectively. The $T(f_m)$ and $T(f_{2m})$ are the transfer functions of the phase-locked-loop (PLL).

The signal frequency shift was obtained by the phase locked loop (PLL) and divided into two parts. One was applied to adjust the tip–sample interaction with a band elimination filter (BEF), and the other was connected to FM-KPFM by feeding it into the lock-in amplifiers. An ac bias voltage was obtained by an oscillator and acted as the reference signal. The f_m and f_{2m} components of the frequency shift were detected by two lock-in amplifiers. As shown in Figure 1, $<I_t>$ was recorded in a separate channel from the tip to cancel the crosstalk, and bias voltage was applied to the sample.

The commercial Ir-coated cantilever (Nanosensors SD-T10L100, f_0 ~800 kHz) was used in the current study. The cantilever tip was first degassed at approximately 650 K for 30 min and then cleaned

by Ar ion bombardment to remove the contaminants, prior to the measurements. Features of the surface structure were related to the charge states of the tip apex, and a stable tip was essential to accurately characterize the surface structure and properties in the experiment [25,26]. The imaging mode became stable in AFM experiments when the metal-coated Si cantilever was employed in the experiments [27–29].
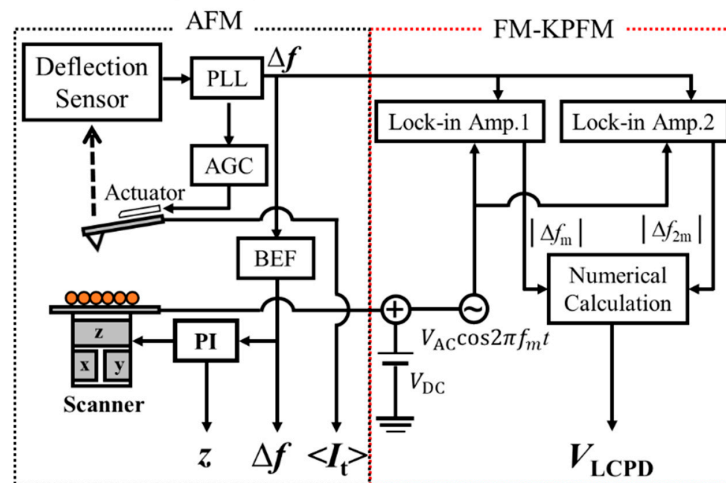

Figure 1. Experimental setup of AFM/FM-KPFM for simultaneous measurements of topography, $<I_t>$ and LCPD.

The $TiO_2(110)$ sample surface (provided by Furuuchi Chemical Corporation, Hyogo, Japan) was prepared by several cycles of Ar ion sputtering and subsequent annealing at 1000 K for 20 min. After that, the freshly cleaned surface was exposed to O_2 in the preparation chamber and then transferred into the observation chamber. AFM images were taken after the sample temperature decreased to 78 K.

3. Results and Discussion

We first introduced the surface structure model of rutile $O-TiO_2$ (110)-(1 × 1) and O_2 dissociation state at room temperature (RT) and 400 K. Figure 2a shows a ball model of the rutile $O-TiO_2$ (110)-(1 × 1) surface, which consists of alternating Ti_{5c} rows and sixfold-coordinated Ti_{6c} rows surrounded by in-plane threefold-coordinated O_{3c} rows and bridging twofold-coordinated O_{2c} rows. The single O_{ad} (O_{ad}: light green ball) formed by O_2 dissociation at the O_v site indicated that one O atom healed O_v and the other located at the Ti_{5c} site, and paired O_{ad} resulted from O_2 dissociation at the Ti_{5c} site.

As reported in the previous literature [30–32], atomic contrast in the AFM image depended on the tip apex polarity, and surface defects were used as markers to distinguish the imaging mode. Hole and protrusion modes usually appeared in the imaging modes. When the tip apex was positively charged, the O_{2c} row was bright on the image due to the larger attractive force between the tip and the negative O_{2c} row. Surface defects were imaged as dark holes, which is called the hole mode [28,29]. When the tip apex was negatively charged, the contrast was inverted compared with that in the hole mode, and H atoms appeared as brighter spots than the O_V defects, which is called the protrusion mode. Figure 2b shows the topography image of the $O-TiO_2(110)$-(1 × 1) surface recorded in the hole mode. According to the experiment, bridging O_{2c} and Ti_{5c} rows were imaged as bright and dark features, respectively, and the bright spots on the Ti_{5c} rows are O_{ad}. As introduced before, the single O_{ad} (denoted by the white dotted circle) was attributed to O_2 dissociation at the O_v site, and paired O_{ad} separated by three lattice distances (denoted by the white dotted oval circle) was the result of O_2 dissociation at the Ti_{5c} site.
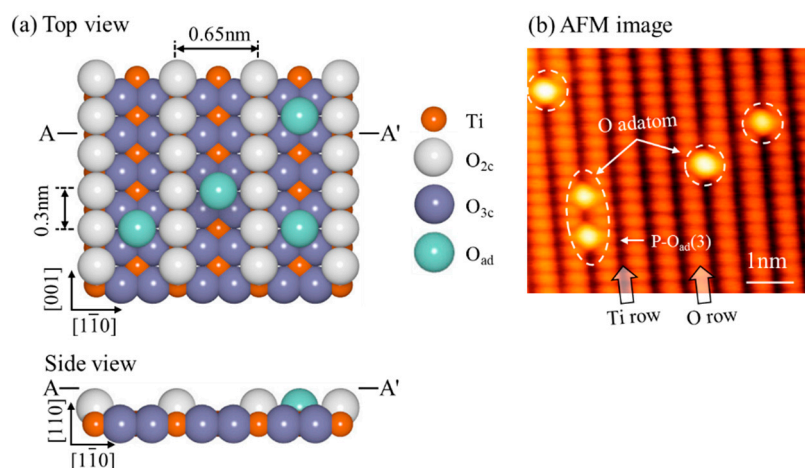
Figure 2. (**a**) Ball model of the rutile O-TiO$_2$(110)-(1 × 1) surface. (Ti$_{5c}$: orange balls, O$_{3c}$: dark blue balls, O$_{2c}$: gray balls, O$_{ad}$: light green balls) (**b**) AFM image of O-TiO$_2$(110)-(1 × 1) surface. Bright and dark rows are O$_{2c}$ and Ti$_{5c}$ rows, respectively, and bright spot is O$_{ad}$. (f_0 = 807 kHz, Q = 23620, Δf = −70 Hz, V_{DC} = 0.6 V and A = 500 pm, image size: 6.3 × 5.3 nm^2).

Figure 3 shows two AFM topographic images of the rutile O-TiO$_2$(110)-(1 × 1) surface exposed to O$_2$ at RT and 400 K, respectively, and the corresponding line profiles along the O$_{ad}$. The contrast is the same as Figure 2b. O$_{2c}$ and Ti$_{5c}$ rows are imaged as bright and dark features, respectively, and the bright spots on the Ti$_{5c}$ rows are O$_{ad}$. Here, paired O$_{ad}$ separated by one lattice constant is denoted as the P-O$_{ad}$(1). As shown in Figure 3a,b and Figure 2b, single O$_{ad}$, P-O$_{ad}$(1), P-O$_{ad}$(2) and P-O$_{ad}$(3) are observed when O$_2$ is exposed to the TiO$_2$ surface at room temperature (RT). As introduced before, single O$_{ad}$ was attributed to O$_2$ dissociation at the O$_v$ site, and paired O$_{ad}$ was the result of O$_2$ dissociation at the Ti$_{5c}$ site. In our results, a single O adatom was the distinctly dominant state of O$_{ad}$, when the exposure temperature was at RT. P-O$_{ad}$(2) is the second preferred state. Density functional theory (DFT) showed the P-O$_{ad}$(2) configuration was the most preferred structure at RT, and further O$_{ad}$ diffusion (P-O$_{ad}$(2) to P-O$_{ad}$(3)) was hindered by a barrier of 1.3 eV [24]. In addition, the separation of P-O$_{ad}$(1) to P-O$_{ad}$(2) was exothermic by 0.4 eV theoretically. P-O$_{ad}$(1) and P-O$_{ad}$(3) configurations were observed in our experiments, but they were rare because separation of O$_{ad}$ is the result of a balance between Coulombic repulsion of two O$_{ad}$ and is thermally driven, and P-O$_{ad}$(1) and P-O$_{ad}$(3) configurations can be generated.

When the sample was exposed to O$_2$ conditions beyond 350 K, dissociated O$_2$ could overcome the diffusion barrier forming the P-O$_{ad}$(3) structure [33]. The number of paired O$_{ad}$ distinctly increased on the O$_2$-exposed surface at 400 K, and the states of the paired O$_{ad}$ were mainly P-O$_{ad}$(3) and P-O$_{ad}$(5) configurations, shown in Figure 3c,d. Under high temperatures for the O$_2$-exposed surface (>400 K), the Ti interstitials (Ti$_{int}$) can diffuse from the bulk to the near-surface region via an interstitial diffusion mechanism [34]. The concentration and distribution of Ti$_{int}$ in the near-surface region can vary significantly, depending on the level of bulk reduction. Current experiments suggest that the excess charge on these paired O$_{ad}$ is mainly provided by the Ti$_{int}$ rather than Ov in determining the adsorption behavior when the O$_2$-exposed surface temperatures went beyond 400 K. Our results demonstrate that O$_2$ dissociatively adsorbed on the rutile TiO$_2$(110)-(1 × 1) surface when the temperature of O$_2$ exposure was at or beyond RT, and results are consistent with the conventional STM observations [24,33]. Next, we explored the O$_{ad}$ on TiO$_2$ surface by AFM/STM.
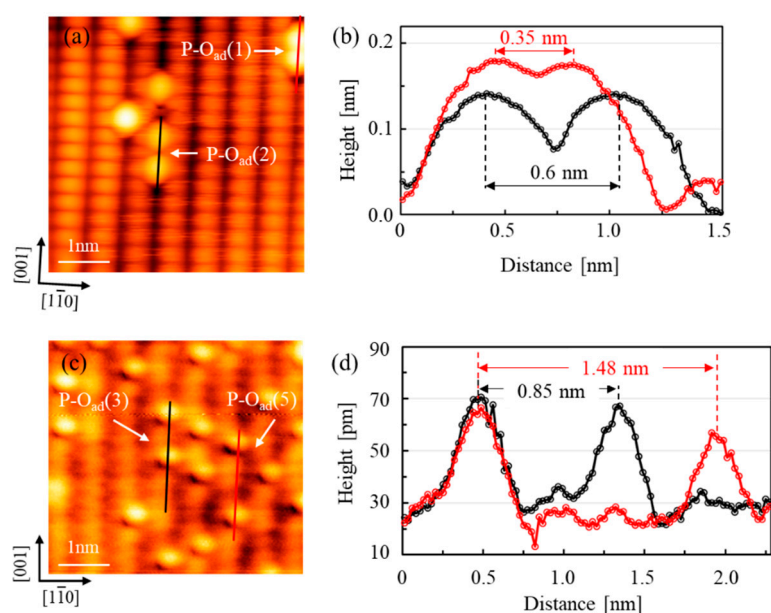
Figure 3. (**a**) AFM images on $TiO_2(110)$ surface. (f_0 = 802 kHz, Q = 13001, Δf = −80 Hz, V_{DC} = 0.4 V, A = 500 pm, 5 × 5 nm^2, O_2 exposure at RT). (**b**) Line profiles along the oxygen adatoms in (**a**). (**c**) AFM images on $TiO_2(110)$ surface. (f_0 = 795 kHz, Q = 6329, Δf = −231 Hz, V_{DC} = 0.4 V, A = 500 pm, 4.5 × 5 nm^2, O_2 exposure at 400K). (**d**) Line profiles along the oxygen adatoms in (**c**).

The four images in Figure 4 are obtained in the same area of the O-$TiO_2(110)$ surface. Figure 4a and 4b experimentally show simultaneously recorded topographic (Z) and $<I_t>$ images recorded in the constant frequency shift mode. In the topographic image (Figure 4a), the atomic contrast is the same as that in Figure 3a, in that the bright and dark rows are the O_{2c} and Ti_{5c} rows, respectively. A bright spot marked by the dashed white circle is O_{ad}. Figure 4b demonstrates the corresponding tunneling current image. Usually, the empty state is imaged at positive sample bias voltage in STM, so O_{2c} and Ti_{5c} rows are imaged as dark and bright rows, respectively, where the contrast of O_{2c} and Ti_{5c} rows is reversed compared with the topographic image. The dark spot marked by the white dashed circle is O_{ad}, and this is different from the conventional STM image of O-$TiO_2(110)$, which is caused by the crosstalk of tip motion. When the tip moves on the O_{ad} site, the additional attractive force acts in the tip–sample interaction, and the tip has to retract in order to keep a constant frequency shift. Thus, tunneling current dramatically decreases, and the contrast of O_{ad} becomes a dark spot in $<I_t>$ image. The bright spot marked by an oval circle is due to subsurface defects, which was not probed in Figure 4a, ever reported by our group or other groups [19,22]. Figure 4c is the Δf image and Figure 4d is the corresponding tunneling current image, recorded in the constant height mode. Compared with Figure 4a,b, the image contrast is the same, except the O_{ad} in Figure 4d. O_{ad} is imaged as bright spot in the $<I_t>$ image due to elimination of the crosstalk between topography and $<I_t>$ signals in the constant height mode. A bright spot and two weak bright spots (denoted by the white square) are observed in Figure 4d, and they are O_{ad} and subsurface defects. It indicates the subsurface defect is not repulsive to O_{ad}. Therefore, AFM/STM is a useful technique to investigate the interaction of the adsorbate and substrate, and constant height operation is necessary. Next, we investigated the O_{ad} by AFM/STM/KPFM.
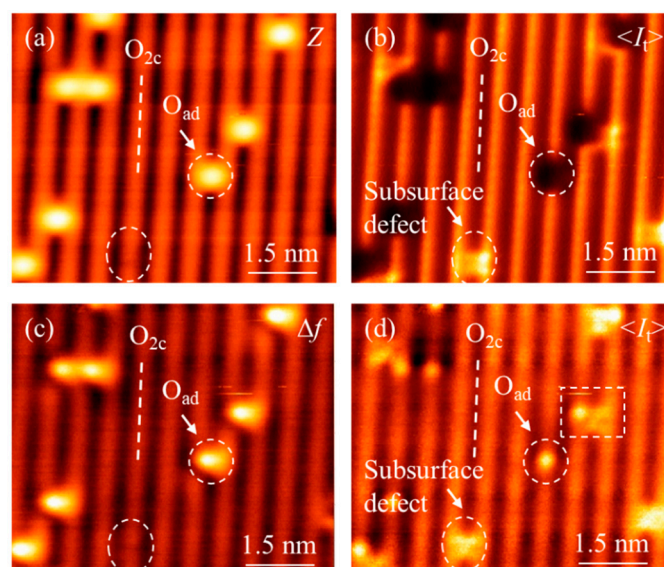
Figure 4. (**a**,**b**) Topographic and corresponding tunneling current images of O-TiO$_2$(110) surface obtained in the constant frequency shift mode. There is crosstalk between topography and $<I_t>$ signals and O$_{ad}$ is imaged dark spot in $<I_t>$ image. (**c**,**d**) frequency shift and corresponding tunneling current images of O-TiO$_2$(110) surface obtained in the constant height mode. The crosstalk between topography and $<I_t>$ signals is eliminated.

Figure 5 shows frequency shift, tunneling current and local contact potential difference images with atomic resolution and corresponding line profiles along the single O$_{ad}$. In the experiment, the measurement was performed in the constant height mode to prevent crosstalk between the signals of the frequency shift and tunneling current. In the Δf image shown in Figure 5a, O$_{2c}$ and Ti$_{5c}$ rows are simultaneously observed as bright rows with super high resolution, and O$_{ad}$ is imaged as the bright spot. In the $<I_t>$ image (see Figure 5b), the contrast was the same as in Figure 5a, except O rows are imaged as dark, which is consistent with the previous studies by conventional STM in that the conduction band of TiO$_2$ is dominated by Ti 3d states, and bright features are usually assigned to the empty Ti 3d states of Ti$_{5c}$ ions under positive sample bias voltage, even though they lie lower than the bridging O$_{2c}$ rows [35]. The tunneling current value on O$_{ad}$ was higher than that on the Ti$_{5c}$ rows, and the current difference between the O$_{ad}$ and Ti$_{5c}$ row was about 0.375 nA. The contrast in STM images depends on the different contributions of Ti 3d and O 2p states and their different decay as a function of the tip–sample separation [36]. O$_{ad}$ is higher than O$_{2c}$ and Ti$_{5c}$ rows in surface geometry, and O$_{ad}$ finally appeared as bright on the image. It was clearly observed that there was some depression around the O$_{ad}$, and this was due to the decreased numbers of empty states near the conduction band for tunneling, which resulted from the negatively charged O$_{ad}$ [24]. This phenomenon was more pronounced in paired O$_{ad}$, as shown in the following tunneling current line profile. In the V_{LCPD} image (see Figure 5c), the imaging contrast was the reverse of that in the image, except for the O$_{ad}$. The relative value of V_{LCPD} between the Ti$_{5c}$ and O$_{2c}$ sites was approximately 28 mV from the line profile (not shown here), and this was in good agreement with our previous studies [18,19]. V_{LCPD} had a higher value on the O$_{ad}$ than on the proximate Ti$_{5c}$ rows, and the relative value of CPD between the O$_{ad}$ and Ti$_{5c}$ row was about 75 mV. It intuitively suggests the electrons transferred from TiO$_2$ to O$_{ad}$.

As shown in Figure 6, line profiles are plotted along the paired O$_{ad}$. The current difference between the O$_{ad}$ and adjacent Ti$_{5c}$ row was about 0.5 nA. The depression between the paired O$_{ad}$ was very pronounced due to the combined effect in the corresponding line profile. The surface potential distribution was also different around the single O adatom and paired O$_{ad}$. The potential difference was 52 mV, as shown in Figure 6b. This indicates the charge state of O$_{ad}$ is different, and excess electrons around the paired O$_{ad}$ are shared by the paired O$_{ad}$ resulting in that the relative value of

CPD between the O_{ad} and Ti_{5c} row is lower. Therefore, multi-channel exploration demonstrates the powerful ability to explore surface properties with SPM.
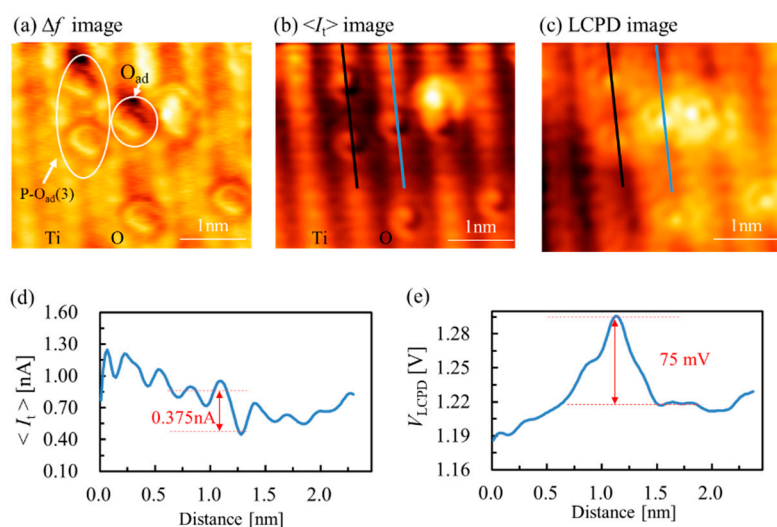

Figure 5. Multiple images of $TiO_2(110)$ surface with atomic resolution and corresponding line profiles. (**a**) Frequency shift (Δf) image, (**b**) tunneling current ($<I_t>$) image and (**c**) local contact potential difference (V_{LCPD}) image. (**d**,**e**) The line profiles along the blue line on the surface in (**b**,**c**). ($f_0 = 805$ kHz, $Q = 27623$, $\Delta f = -260$ Hz, $V_{DC} = 1.3$ V, $V_{AC} = 1.5$ V, $A = 500$ pm, size: 3.5×3.2 nm^2).
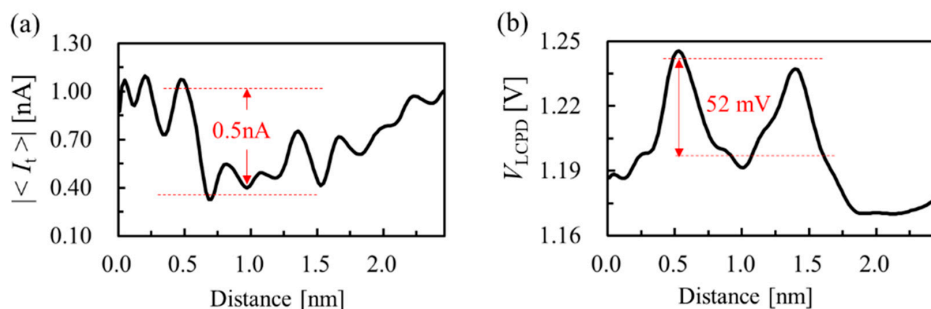
Figure 6. The line profiles along the dark line on the surface in Figure 5b,c. (**a**) Tunneling current and (**b**) local contact potential difference line profiles along the paired O adatoms.

4. Conclusions

We studied the O_2 dissociated state under different O_2-exposed sample surfaces with high resolution, and we investigated the electron charge transfer between the adsorbed O and TiO_2 substrate with multi-channel exploration. We observed the interaction between O_{ad} and the subsurface, and we confirmed the electron charge transfer from the TiO_2 surface to the adsorbed O upon O_2 dissociation on the $TiO_2(110)$ surface by tunneling current and local contact potential difference. Our results demonstrated that multi-channel exploration was able to obtain the surface structures and charge transfers between the adsorbate and substrate, and this is expected to be useful for investigating the surface properties and charge transfer phenomena at the interface.

References

1. Sugimoto, Y.; Pou, P.; Custance, O.; Jelinek, P.; Abe, M.; Perez, R.; Morita, S. Complex patterning by vertical interchange atom manipulation using atomic force microscopy. *Science* **2008**, *322*, 413–417. [CrossRef] [PubMed]

2. Gross, L.; Mohn, F.; Moll, N.; Liljeroth, P.; Meyer, G. The chemical structure of a molecule resolved by atomic force microscopy. *Science* **2009**, *325*, 1110–1114. [CrossRef] [PubMed]

3. Zhang, J.; Chen, P.C.; Yuan, B.K.; Ji, W.; Cheng, Z.; Qiu, X.H. Real-space identification of intermolecular bonding with atomic force microscopy. *Science* **2013**, *342*, 611–614. [CrossRef] [PubMed]

4. Guo, J.; Meng, X.Z.; Chen, J.; Peng, J.B.; Sheng, J.M.; Li, X.Z.; Xu, L.M.; Shi, J.R.; Wang, E.G.; Jiang, Y. Real-space imaging of interfacial water with submolecular resolution. *Nat. Mater.* **2014**, *13*, 184–189. [CrossRef] [PubMed]

5. Bamidele, J.; Lee, S.H.; Kinoshita, Y.; Turansky, R.; Naitoh, Y.; Li, Y.J.; Sugawara, Y.; Stich, I.; Kantorovich, L. Vertical atomic manipulation with dynamic atomic-force microscopy without tip change via a multi-step mechanism. *Nat. Commun.* **2014**, *5*, 4476. [CrossRef] [PubMed]

6. Jiang, P.; Bao, X.; Salmeron, M. Catalytic reaction processes revealed by scanning probe microscopy. *Acc. Chem. Res.* **2015**, *48*, 1524–1531. [CrossRef] [PubMed]

7. Kim, H.; Kyhm, K.; Taylor, R.A.; Kim, J.S.; Song, J.D.; Park, S. Optical shaping of the polarization anisotropy in a laterally coupled quantum dot dimer. *Light Sci. Appl.* **2020**, *9*, 100. [CrossRef]

8. Jiang, S.; Zhang, X.; Zhang, Y.; Hu, C.; Zhang, R.; Zhang, Y.; Liao, Y.; Smith, Z.J.; Dong, Z.; Hou, J.G. Subnanometer-resolved chemical imaging via multivariate analysis of tip-enhanced Raman maps. *Light Sci. Appl.* **2017**, *9*, e17098. [CrossRef]

9. Wen, H.F.; Zhang, Q.; Yuuki, A.; Miyazaki, M.; Naitoh, Y.; Li, Y.J.; Sugawara, Y. Direct visualization of oxygen reaction with paired hydroxyl on $TiO_2$110 surface at 78 K by atomic force microscopy. *J. Phys. Chem. C* **2018**, *122*, 17395–17399. [CrossRef]

10. Adachi, Y.; Wen, H.; Zhang, Q.; Miyazaki, M.; Sugawara, Y.; Sang, H.; Brndiar, J.; Kantorovich, L.; Štich, I.; Li, Y.J. Tip-induced control of charge and molecular bonding of oxygen atoms on the rutile $TiO_2$110 surface with atomic force microscopy. *ACS Nano* **2019**, *13*, 6917–6924. [CrossRef]

11. Melitz, W.; Shen, J.; Kummel, A.C.; Lee, S. Kelvin probe force microscopy and its application. *Surf. Sci. Rep.* **2011**, *66*, 1–27. [CrossRef]

12. Wandelt, K. The local work function: Concept and implications. *Appl. Surf. Sci.* **1997**, *111*, 1–10. [CrossRef]

13. Albrecht, T.R.; Grütter, P.; Horne, D.; Rugar, D. Frequency modulation detection using high-Q cantilevers for enhanced force microscope sensitivity. *J. Appl. Phys.* **1991**, *69*, 668–673. [CrossRef]

14. Sugawara, Y.; Kou, L.; Ma, Z.; Kamijo, T.; Naitoh, Y.; Li, Y.J. High potential sensitivity in heterodyne amplitude-modulation Kelvin probe force microscopy. *Appl. Phys. Lett.* **2012**, *100*, 223104. [CrossRef]

15. Ma, Z.M.; Kou, L.; Naitoh, Y.; Li, Y.J.; Sugawara, Y. The stray capacitance effect in Kelvin probe force microscopy using FM, AM and heterodyne. *Nanotechnology* **2013**, *24*, 225701. [CrossRef]

16. Ziegler, D.; Stemmer, A. Force gradient sensitive detection in lift-mode Kelvin probe force microscopy. *Nanotechnology* **2011**, *22*, 075501. [CrossRef]

17. Takeuchi, O.; Ohrai, Y.; Yoshida, S.; Shigekawa, H. Kelvin Probe Force Microscopy without Bias-Voltage Feedback. *Jpn. J. Appl. Phys.* **2007**, *46*, 5626–5630. [CrossRef]

18. Kou, L.; Ma, Z.; Li, Y.J.; Naitoh, Y.; Komiyama, M.; Sugawara, Y. Surface potential imaging with atomic resolution by frequency-modulation Kelvin probe force microscopy without bias voltage feedback. *Nanotechnology* **2015**, *26*, 165701. [CrossRef]

19. Wen, H.F.; Li, Y.J.; Arima, E.; Naitoh, Y.; Sugawara, Y.; Xu, R.; Cheng, Z.H. Investigation of tunneling current and local contact potential difference on the TiO_2(110) surface by AFM/KPFM at 78 K. *Nanotechnology* **2017**, *28*, 105704. [CrossRef]

20. Ashino, M.; Sugawara, Y.; Morita, S.; Ishikawa, M. Atomic resolution noncontact atomic force and scanning tunneling microscopy of $TiO_2(110)$-(1×1) and (1×2): Simultaneous imaging of surface structures and electronic states. *Phys. Rev. Lett.* **2001**, *86*, 4334–4337. [CrossRef]

21. Sugimoto, Y.; Nakajima, Y.; Sawada, D.; Morita, K.I.; Abe, M.; Morita, S. Simultaneous AFM and STM measurements on the Si(111)-(7×7) surface. *Phys. Rev. B* **2010**, *81*, 245322. [CrossRef]

22. Baykara, M.Z.; Mönig, H.; Schwendemann, T.C.; Ünverdi, Ö.; Altman, E.I.; Schwarz, U.D. Three-dimensional interaction force and tunneling current spectroscopy of point defects on rutile $TiO_2(110)$. *Appl. Phys. Lett.* **2016**, *108*, 071601. [CrossRef]

23. Wang, Z.T.; Deskins, N.A.; Lyubinetsky, I. Direct imaging of site-specific photocatalytical reactions of O_2 on $TiO_2(110)$. *J. Phys. Chem. Lett.* **2012**, *3*, 102. [CrossRef]

24. Du, Y.; Deskins, N.A.; Zhang, Z.; Dohnalek, Z.; Dupuis, M.; Lyubinetsky, I. Formation of O adatom pairs and charge transfer upon O_2 dissociation on reduced $TiO_2(110)$. *Phys. Chem. Chem. Phys.* **2010**, *12*, 6337–6344. [CrossRef] [PubMed]

25. Naitoh, Y.; Kinoshita, Y.; Li, Y.J.; Kageshima, M.; Sugawara, Y. The influence of a Si cantilever tip with/without tungsten coating on noncontact atomic force. *Nanotechnology* **2009**, *20*, 264011. [CrossRef]

26. Li, Y.J.; Wen, H.F.; Naitoh, Y.; Sugawara, Y. Stable contrast mode on $TiO_2 110$ surface with metal-coated tip using AFM. *Ultramicroscopy* **2018**, *191*, 51–55. [CrossRef]

27. Zhang, Q.; Li, Y.J.; Wen, H.F.; Adachi, Y.; Miyazaki, M.; Sugawara, Y.; Xu, R.; Cheng, Z.H.; Brndiar, J.; Kantorovich, L.; et al. Measurement and manipulation of the charge state of an adsorbed oxygen adatom on the rutile $TiO_2(110)$-(1×1) surface by nc-AFM and KPFM. *J. Am. Chem. Soc.* **2018**, *140*, 15668–15674. [CrossRef]

28. Wen, H.F.; Yuuki, A.; Zhang, Q.; Miyazaki, M.; Li, Y.J.; Sugawara, Y. Identification of atomic defects and adsorbate on rutile $TiO_2(110)$-(1×1) surface by atomic force microscopy. *J. Phys. Chem. C* **2019**, *123*, 25756–25760. [CrossRef]

29. Wen, H.F.; Zhang, Q.; Yuuki, A.; Miyazaki, M.; Sugawara, Y.; Li, Y.J. Contrast inversion of O adatom on rutile $TiO_2(110)$-(1×1) surface by atomic force microscopy imaging. *App. Surf. Sci.* **2020**, *505*, 144623. [CrossRef]

30. Lauritsen, J.V.; Foster, A.S.; Olesen, G.H.; Christensen, M.C.; Kühnle, A.; Helveg, S.; Rostrup-Niesen, J.R.; Clausen, B.S.; Reichling, M.; Besenbacher, F. Chemical identification of point defects and adsorbates on a metal oxide surface by atomic force microscopy. *Nanotechnology* **2006**, *17*, 3436. [CrossRef]

31. Yurtsever, A.; Sugimoto, Y.; Abe, M.; Morita, S. NC-AFM imaging of the $TiO_2 110$-1×1 surface at low temperature. *Nanotechnology* **2010**, *21*, 165702. [CrossRef] [PubMed]

32. Bechstein, R.; González, C.; Schütte, J.; Jelínek, P.; Pérez, R.; Kühnle, A. 'All-inclusive' imaging of the rutile$TiO_2(110)$ surface using NC-AFM. *Nanotechnology* **2009**, *20*, 505703. [CrossRef]

33. Lira, E.; Hansen, J.Ø.; Huo, P.; Bechstein, R.; Galliker, P.; Lægsgaard, E.; Hammer, B.; Wendt, S.; Besenbacher, F. Dissociative and molecular oxygen chemisorption channels on reduced rutile $TiO_2(110)$: An STM and TPD study. *Surf. Sci.* **2010**, *604*, 1945–1960. [CrossRef]

34. Wendt, S.; Sprunger, P.T.; Lira, E.; Madsen, G.K.; Li, Z.; Hansen, J.Ø.; Matthiesen, J.; Blekinge-Rasmussen, A.; Lægsgaard, E.; Hammer, B.; et al. The role of interstitial sites in the Ti3d defect state in the band gap of titania. *Science* **2008**, *320*, 1755. [CrossRef] [PubMed]

35. Minato, T.; Sainoo, Y.; Kim, Y.; Kato, H.S.; Aika, K.I.; Kawai, M.; Zhao, J.; Petek, H.; Huang, T.; He, W.; et al. The electronic structure of oxygen atom vacancy and hydroxyl impurity defects on titanium dioxide 110 surface. *J. Chem. Phys.* **2009**, *130*, 124502. [CrossRef]

36. Woolcot, T.; Teobaldi, G.; Pang, C.L.; Beglitis, N.S.; Fisher, A.J.; Hofer, W.A.; Thornton, G. Scanning tunneling microscopy contrast mechanisms for TiO_2. *Phys. Rev. Lett.* **2012**, *109*, 156105. [CrossRef]